Additive Manufacturing 39 (2021) 101644

Contents lists available at ScienceDirect

Additive Manufacturing

journal homepage: www.elsevier.com/locate/addma

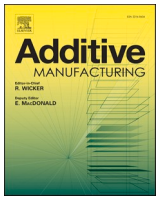

Research Paper

# Electrostatically-assisted direct ink writing for additive manufacturing

J. Plog, Y. Jiang, Y. Pan *, A.L. Yarin *

*Department of Mechanical and Industrial Engineering, University of Illinois at Chicago, 842 W. Taylor St., Chicago, IL 60607-7022, USA*

A B S T R A C T

Nozzle-based three-dimensional (3D) printing (additive manufacturing) technologies, which build a model by depositing and stacking materials layer-by-layer, are limited by long layer-build time resulting in low throughput. While nozzle-based printing is already arguably versatile, such sub-categories as Direct-Ink-Writing (DIW) find difficulty when printing material on rough surfaces. Recently electrohydrodynamic (EHD) elements added new features in droplet positioning but also revealed limitations in the achievable build height due to the need for a grounded substrate or embedded electrode. Here, we introduce an additional electrode added to the printhead generating an electric field (E.F.) between the above-mentioned electrode and printing nozzle. The resulting Coulomb force pulls the extruded ink in the direction of printing allowing faster translational speed, thinner trace widths, and improved deposition on rough surfaces without a decrease throughout the build height. We also developed the electrohydrodynamic theory of the proposed DIW processes. After completing DIW experiments on a translating belt with a stationary nozzle, an electric field oriented in the direction of printing was retrofitted to a DIW-based 3D printer. The integration of the electrode to the printhead allowed successful prints at the machine's maximum speed of 500 mm/s for a documented situation in which DIW previously failed in existing literature. Similarly, successful prints were achieved on rough surfaces where the printing was impossible without the applied E.F. Along with new design opportunities, these results unlock speed restriction within nozzle-based printing while significantly expanding versatility and substrate choices. Compared to the state-of-the-art DIW processes, our electrostatically-assisted direct ink writing technology shows orders of magnitude faster direct writing speed (> 500 mm/s) and capability of printing on super-rough surfaces which were impossible before.

## 1. Introduction

Dispensing liquid jets are used in a vast range of industrial applications, including additive manufacturing (AM), surface coating and dispensing cooling [1]. Many of these applications are linked by the common underlying physical phenomena. Within the broad scope of AM, many manufacturing advantages have been demonstrated, including freedom of structural design, reduced concept-to-completion time, and minimized waste [2–4]. Specifically, nozzle-based continuous filament extrusion AM technologies possess the ability to print a wide range of materials including but not limited to metals, synthetic and natural polymers, ceramics and bio-gels [5–8], and in many cases more effectively than dripping-based approach [9].

One such nozzle-based AM technology is Direct Ink Writing (DIW) which is also synonymous with Robocasting (robotic material extrusion). DIW is described by Chrisey and Piqué [10] as "any technique or process capable of depositing, dispensing or processing different types of materials over various surfaces following a preset pattern or layout". While the concept of extruding functional fluids through a nozzle to digitally defined locations is decades-old, new applications in printed electronics continue to widen DIW as an emerging field. Jiang et al [11] summarized the recent advances by stating that DIW provides a "bright opportunity for electronic systems" due to functional materials. There is at best a quasi-understanding of the complex jetting and impact dynamics involved, which becomes increasingly salient as jetting technologies proliferate into an evolving and demanding industry [1,12–14].

Modern application and forthcoming ideas impose extreme demands on DIW systems requiring ever increasing speed and wider substrate choices, while maintaining precision and reliable functioning. One problem with DIW is that an increased relative velocity between nozzle and substrate causes more manufacturing defects [14], such as bulging, discontinued lines, liquid puddles, liquid splashing and coffee-ring effects [15–24], therefore limiting the printing speed. Besides, the printing resolution is limited by the inner diameter (I.D.) of the dispensing needle in the DIW system. To achieve a good printing accuracy, the dispensing needle is usually located close to the substrate at a distance which is called standoff distance (S.D.). In reality, the S.D. is proportional to the printing orifice diameter and is typically set between 50% and 100% the needles' I.D. With DIW needles' often being on the order of 50–100 μm, attempting to maintain a microscale standoff distance proves problematic and has previously limited prints to very smooth substrates and low speeds (0.1–100 mm/s) [25].

In the current booming AM market, speed is valued on a similar magnitude as resolution and cost. As novel ideas [e.g., application of

* Corresponding authors.
*E-mail addresses:* yayuepan@uic.edu (Y. Pan), ayarin@uic.edu (A.L. Yarin).

https://doi.org/10.1016/j.addma.2020.101644
Received 25 July 2020; Received in revised form 16 September 2020; Accepted 25 September 2020
Available online 12 October 2020

electric fields (E.F.) to enhance printing] arise, the underlying physics is often re-examined, seeking gains in either speed or resolution and the reduction of cost, albeit rarely all three. Liashenko et al. [26] showed that ink could be pulled and deflected from a nozzle by applying several E.F.s. The first E.F., applied between needle and substrate, facilitates DIW with electrohydrodynamic (EHD) jetting. EHD electrostatically pulls the ink from the needle to substrate as the liquid meniscus shapes into a modified Taylor cone with a jet issued from its tip [27–29]. Numerous studies have shown EHD jetting capable of printing sub-micrometer features from nanometer-sized jets with minimal risk of clogging [30]. Further facilitating this process with two additional electrodes placed between the needle and substrate, Liashenko et al. [26] were able to electrostatically deflect a jet to create sub-micrometer features with translating print speeds up to 500 mm/s, albeit only for traces less than 2 mm in length. It should be emphasized that because the EHD process depends on the distance between the charged nozzle and the grounded electrode beneath the substrate, the effects of the E.F. would diminish as build height increases. Accordingly, this approach is not well-suited for multi-layer deposition for productions of 3D models. Another attempt to increase the speed of EHD line-printing stems from the addition of different polymers to affect jet behavior. Phung et al. [31] demonstrated promising results with adding polymer to ink to increase the printing speed in a specific case from 10 to 50 mm/s for continuous line-printing. However, the addition of polymers to inks is rarely preferred when not absolutely necessary.

The present work aims to address the above challenges in printing speed, resolution, material choices, and limited layer numbers. We propose to modify the conventional DIW process with a strategically applied electric field set to pull the ink jet footprint on the moving substrate in the direction opposite to that of relative substrate motion. We also develop the theory of the conventional DIW process and its modification with the electric field. In this work, the governing electrode is mounted on the printhead, and as a result, the effects of the E.F. do not diminish as the build height increases. The experimental setup is discussed in Section 2. The experiments performed to study the practical application of an E.F. to the jetting characteristics of DIW are presented and discussed in Section 3. The theory is developed and compared with the experimental data in Section 4. Conclusions are drawn in Section 5.

## 2. Experimental setup

To study the effects of the E.F. on the perpendicular dispensing of a circular jet onto a horizontally translating substrate, the setup sketched in Fig. 1 was designed and built. The defining characteristic of this setup is the ability to translate the substrate beneath the nozzle and the governing electrode. This model setup mimics one of the degrees of freedom found in dispensing robots and ink-jet systems. This layout is used to facilitate video recording of the writing process. A high-voltage power supply provides a ground to the printing needle while it positively charges the governing electrode placed behind the needle relative to the direction of the substrate motion. This governing electrode would always pull the ink in the direction opposite to that of the substrate motion. To generate a driving pressure, a commercial pressure controller (Nordson Ultimus I) supplemented with 27, 30, 32 and 34-gauge stainless steel printing needles is used in this setup. This system allowed for a well-defined pressure pulse (1–80 psi) to be applied to the ink within the needle for a specific time. The governing electrode was produced from a 0.5 mm copper wire bent into a position not to extend below the printing needle edge.

To explore the effect of the ink viscosity in the DIW process, a water jet is compared to a more viscous jet comprised of a solution of 60 wt% of sugar in water. A commercial DIW ink (Spot-E) was purchased from Spot-A materials to explore the effect of the E.F. Voltages applied to the governing electrode were in the 2–4 kV range with the E.F. strength being limited to ~ 3 kV/mm by the dielectric breakdown of air. After initial experiments, the setup depicted in Fig. 1 was retrofitted to a DIW (Direct-Ink-Writing) automated dispensing system, as shown in Fig. 2.

One 0.5 mm copper electrode was attached to a custom dielectric printhead placing the printer's needle inline with the electric field. To

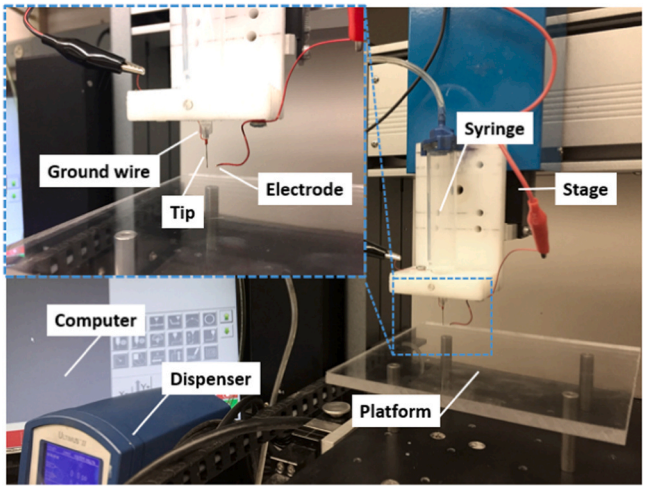


**Fig. 2.** Photo of retrofitted DIW (Direct-Ink-Writing) automated dispensing system setup utilizing perpendicular dispensing of a circular jet onto a translating substrate enhancing deposition by means of the applied E.F.

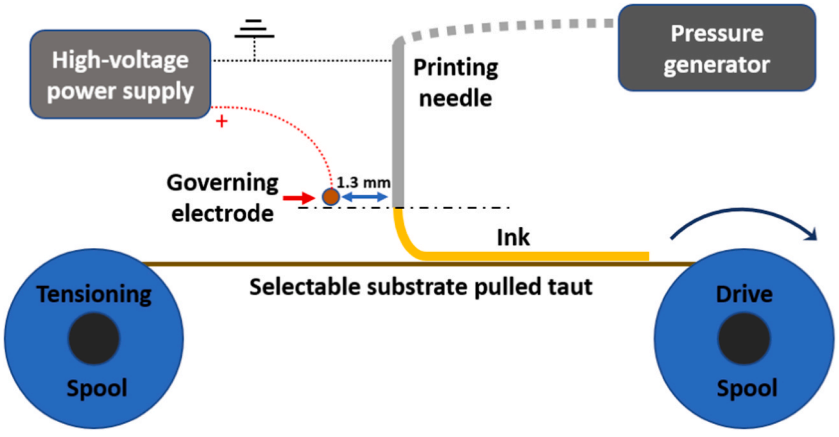


**Fig. 1.** Schematic of the experimental setup utilizing the perpendicular dispensing of a circular jet onto a translating substrate A voltage applied to the governing electrode is used to facilitating smooth and speedy ink deposition by means of the E.F.

demonstrate the feasibility of this approach for ultra-fast line printing, a simple pattern with 10 cm in length was printed with 5 replicates in random order both with and without the applied E.F. at the line speed in the 50–500 mm/s range. The continuous filament extrusion and deposition was captured using a high-speed CCD camera (Phantom V210) using back-light shadowgraphy. All experiments were performed under ambient conditions.

## 3. Experimental results and discussion

### 3.1. Perpendicular dispensing of jet without electric field

With all variables held constant except the belt velocity, Fig. 3 shows the dispensing of water at an estimated velocity of 1030 mm/s with belt speeds of 20 mm/s (Fig. 3a) and 100 mm/s (Fig. 3b). While a slight decrease in the advancement of lamella (the jet footprint) against the substrate motion is noticed at the increased belt speed, the low viscosity of water (0.97 cP at 21.1 °C) allows a relatively easy spreading and wettability-driven advancement of the three-phase contact line against the direction of the belt motion.

In DIW, the ink viscosity is often several orders of magnitude higher than that of water. Accordingly, a model fluid, a solution of 60 wt% of sugar in water was prepared (the viscosity of 7.81 cP at 21.1 °C). With an increase in viscosity, there is no longer lamellae advancement against the direction of the belt motion even at the lowest belt speed. Fig. 4 shows the steady-state locations of the three-phase contact line at two different belt speeds: 20 mm/s in Fig. 4a and 40 mm/s in Fig. 4b. Fig. 4c shows the transient state, with the jet being stretched by the belt travelling at 60 mm/s until the trace line breaks up resulting in discrete droplets.

### 3.2. Jet with electric field applied

To investigate the influence of the E.F. on the jet, a fixed belt velocity, standoff distance, and pressure were used in the following experiments. Without the electric field, the belt wetting by the impacting jet is mainly affected by the belt speed and the flow rate in the jet (cf. Section 3.2). The jet impacts onto the belt and forms a liquid path, which also might break up into individual drops under the action of surface tension. The applied E.F. affects the jet behavior, as well as the wetting of the surface. The jet and advancing triple line are pulled toward the governing high-voltage electrode, thus, facilitating lamella motion against the direction of the belt motion. For a high electric field strength, the viscous solution readily spreads over the belt against the direction of its motion reducing and/or completely eliminating the offset between the triple line and the jet axis (cf. Fig. 4). This diminishes dramatically the propensity to formation of discrete droplets. The electrically-facilitated holding of the triple line near the jet axis allows higher belt speeds at steady-state operation, i.e., allows an increase in the printing velocity compared to the comparable control case without E.F. Fig. 5 shows the E.F.-facilitated pulling of the lamella (jet footprint) triple line against the direction of the belt motion by electrowetting. Such a new steady-state location of the triple line slightly before the jet axis rather than behind it significantly stabilizes the direct writing process of the 60 wt% sugar solution in water extruded through a 30-gauge blunt needle. Both Fig. 5a and b depict steady-state configurations, with the only difference being the applied E.F. with a strength of 2.5 kV/mm to the governing electrode in Fig. 5b. It is clear that in the reverse motion of a dispensing robot the E.F. pulls the jet and lamella triple line in the printing direction eliminating the drag-off distance, which is seen in Fig. 5a and eliminated in Fig. 5b.

To further explore the effect of the E.F. on DIW, a commercial ink Spot-E purchased from Spot-A materials was loaded into the barrel syringe and extruded through a 34-gauge needle at 30 psi. A relatively smooth Mylar (polyethylene terephthalate) ribbon with a surface roughness estimated as $R_a \leq 10$ μm was loaded into the belt drive, as in Figs. 3–5. Fig. 6a shows an intact Spot-E trace line being printed at 40 mm/s with no electric field applied, albeit the drag-off distance is large. The application of the E.F. (2.5 kV/mm) in Fig. 6b reveals a similar trend to that observed with the 60 wt% sugar/water solution, i.e., reduction of the drag-off distance accompanied by a smooth steady-state print. Doubling the belt speed to 80 mm/s, Fig. 6c reveals a problematic printing state where the trace line fails to stay intact, and discrete puddles are left on the surface of the Mylar ribbon. Fig. 6d confirms that the intact-line printing at this speed is achievable with the addition of the E.F. of 2.5 kV/mm.

With print improvement achieved and recorded at S.D. less than or equal to the diameter of the printing nozzle (cf. Figs. 5 and 6), the effect of the E.F. on DIW at elevated S.D. was explored. Fig. 7a–d shows a series of snapshots taken at different S.D. of 80, 240, 380 and 600 μm, respectively. The results show that a strategically applied E.F. would allow a DIW machine printing at the surface to lift its needle and clear an obstacle without disturbing an intact-line printing. This demonstration of reduction of DIW sensitivity to S.D. is an associated benefit of electrowetting.

While the width of the trace line from a DIW machine is most often on the same order of magnitude as the I.D. of the printing needle, the ability to raise the needle if an E.F. is applied, allows DIW printers to reduce their trace width compared to a trace line printed at the same flowrate and no E.F. applied.

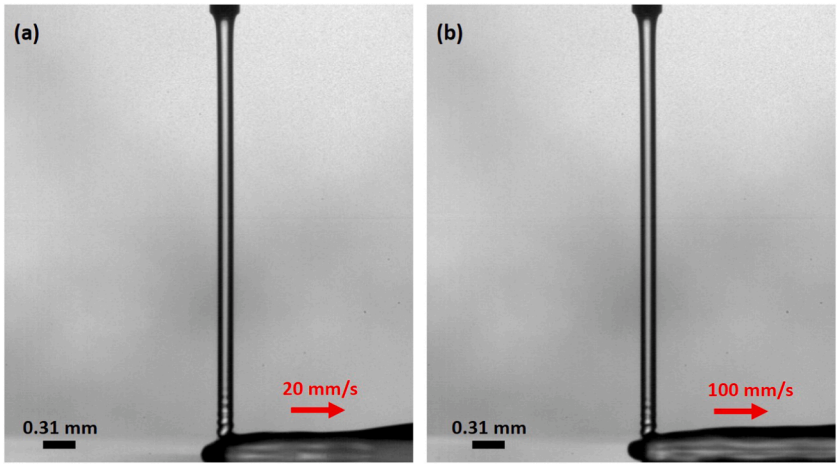


**Fig. 3.** Water dispensing at ~ 1030 mm/s onto Mylar belt (polyethylene terephthalate at 0.019 mm in thickness), which is partially wettable by water, with the contact angle of ~ 35–40°. Belt speed equals: (a) 20 mm/s (b) 100 mm/s.

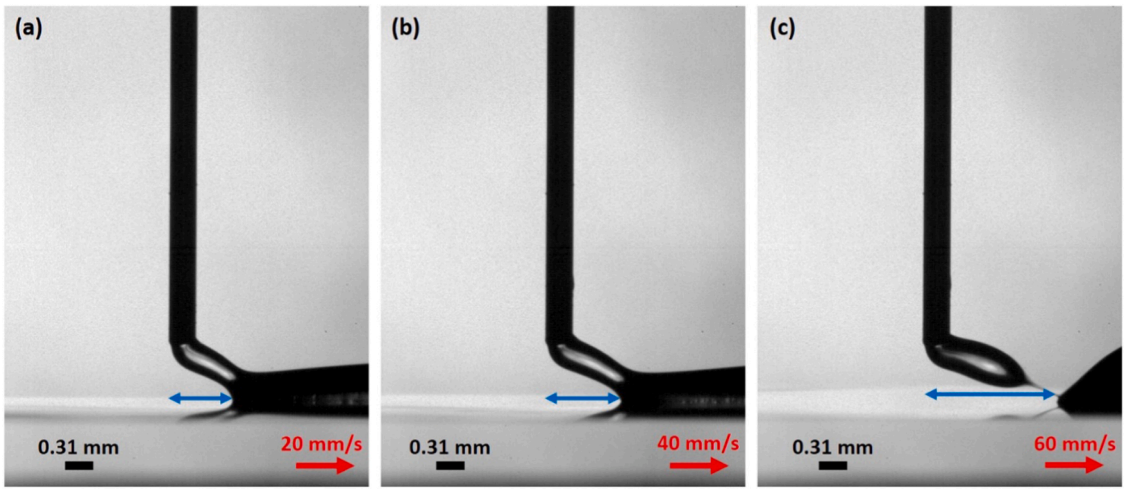


**Fig. 4.** Solution of 60 wt% of sugar in water issued at ~ 380 mm/s: all figures depict a steady or cyclical steady state. (a) 20 mm/s belt speed. (b) 40 mm/s belt speed. (c) 60 mm/s belt speed; cyclical steady state resulting in discrete droplet formation on the belt. Blue arrows show the displacement of the triple line from the jet axis. (For interpretation of the references to color in this figure legend, the reader is referred to the web version of this article.)

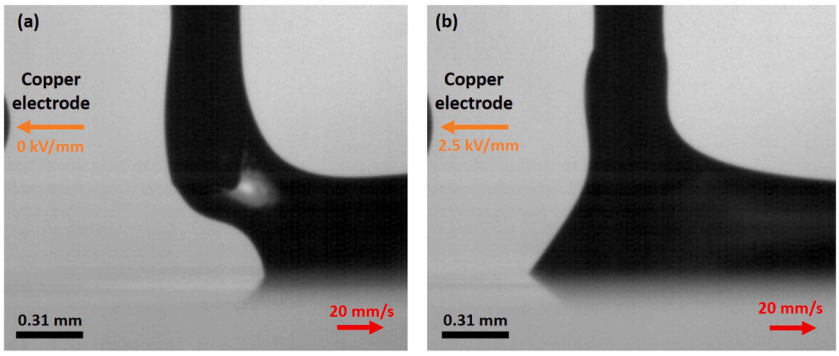


**Fig. 5.** Images of 60 wt% sugar solution in water issued from the nozzle at ~ 380 mm/s at a 20 mm/s belt speed. (a) no E.F. – 0 kV/mm (b) E.F. of 2.5 kV/mm.

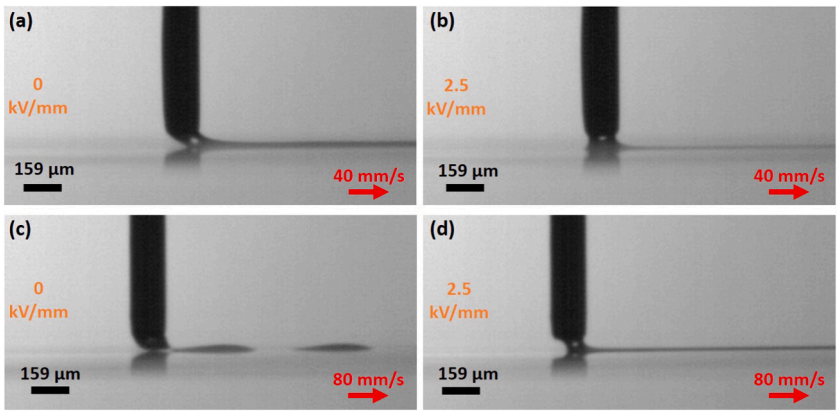


**Fig. 6.** Spot-E printed at ~ 2 mm/s from the nozzle onto Mylar belt at two different belt speeds without and with the E.F. of 2.5 kV/mm applied to the governing electrode (not seen shown in the snapshots). (a) 40 mm/s belt speed, 0 kV/mm. (b) 40 mm/s belt speed, 2.5 kV/mm. (c) 80 mm/s belt speed, 0 kV/mm. (d) 80 mm/s belt speed, 2.5 kV/mm.

Fig. 8a and b highlight the change in the trace line thicknesses resulting from a change in the S.D., while Fig. 8b and c show the effect of an increased flow rate as the driving pressure was increased from 30 to 60 psi at the same S.D.

In DIW prints, the standoff distance between the needle and substrate are held to a high tolerance to avoid printing defects and failures. Typically, in DIW, the S.D. throughout the print varies by less than 10% of the original S.D. set at the beginning of printing. In contrast, the present research explored extreme cases. By deflecting the Mylar ribbon on the belt-drive apparatus, an abnormally large S.D. deviation was administered during the print. Fig. 9a–c show three sequential snapshots corresponding respectively to before, at and after the obstacle. It is seen that even with a relatively large variation in S.D. (which corresponds to the case of rough surfaces), a continuous and uniform trace was

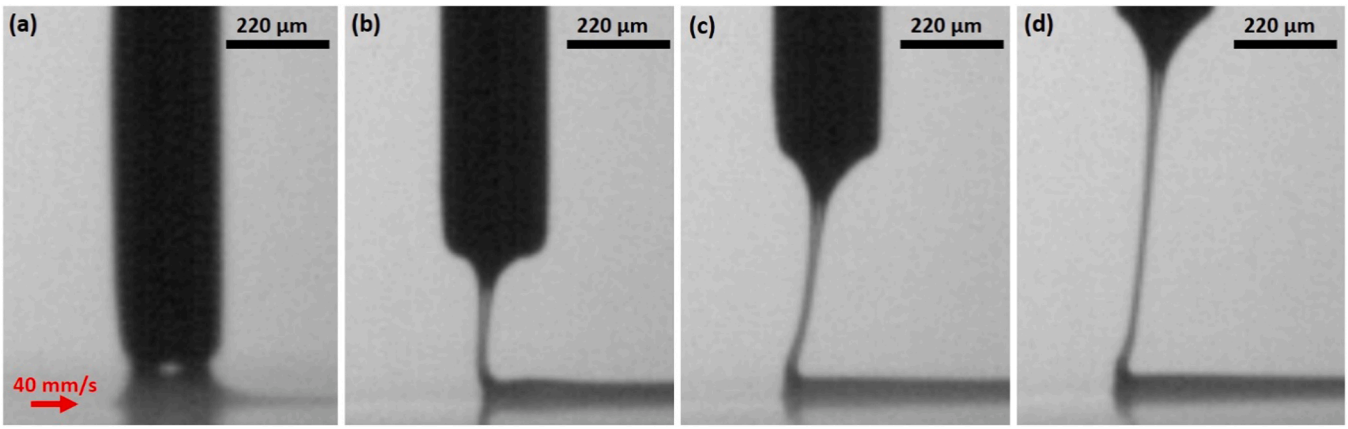


**Fig. 7.** Spot-E extruded at ~ 2 mm/s from 34-gauge needle at 30 psi with a 40 mm/s belt speed and 2.5 kV/mm applied voltage at the governing electrode (not seen in the snapshots). Only the stand-off distance (S.D.) is changed. (a) S.D. ~ 80 µm. (b) S.D. ~ 240 µm. (c) S.D. ~ 380 µm. (d) S.D. ~ 600 µm.

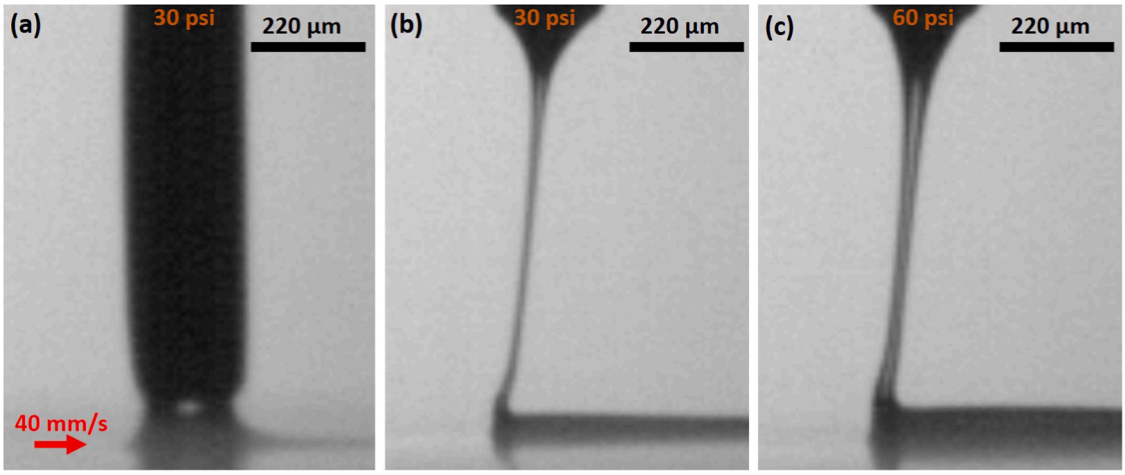


**Fig. 8.** Spot-E extruded from 34-gauge needle with a 40 mm/s belt speed and 2.5 kV/mm applied voltage at the governing electrode (not seen in the snapshots). (a) S.D. ~ 80 µm, 30 psi, jet velocity ~ 2 mm/s. (b) S.D. ~ 600 µm, 30 psi, jet velocity ~ 2 mm/s. (c) S.D. ~ 600 µm, 60 psi, jet velocity ~ 4 mm/s.

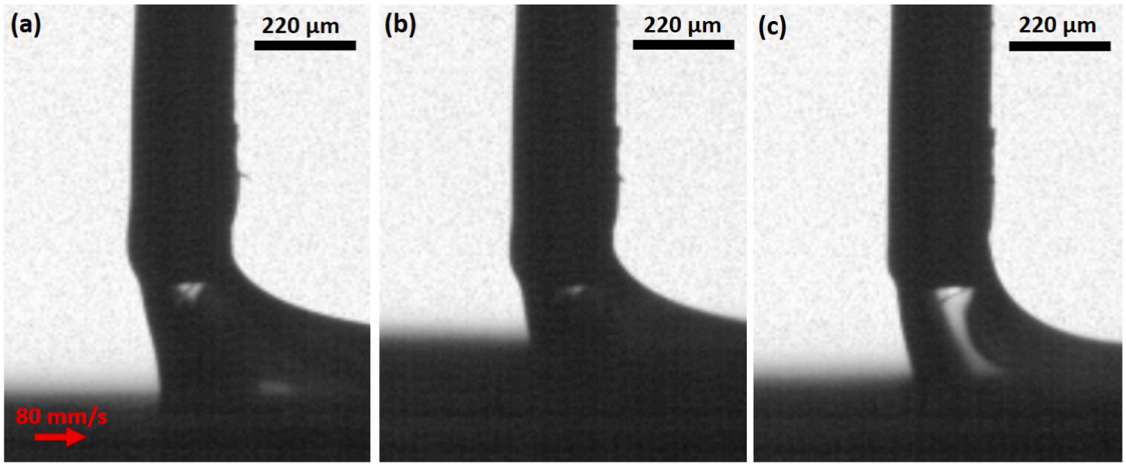


**Fig. 9.** Spot-E extruded at ~ 2 mm/s from 34-gauge needle with the 80 mm/s belt speed, 30 psi and 2.5 kV/mm applied voltage at the governing electrode (not seen in the snapshots). (a) Before, (b) at, (c) after the obstacle.

deposited on the translating belt in all the three cases.

The following Fig. 10 shows the transient effects accompanying turning off the E.F. in the case of Spot-E ink DIW on the Mylar belt. Fig. 10a shows the initial time moment when the electric potential was turned off at $t \approx 0$ s. Fig. 10b shows the development of the drag-off distance already at $t \approx 0.25$ s. Then, at $t \approx 0.5$ s, the triple line of the lamellar footprint of the jet already swept by the moving belt quite significantly, reaching a final steady-state position at $t \approx 1$ s.

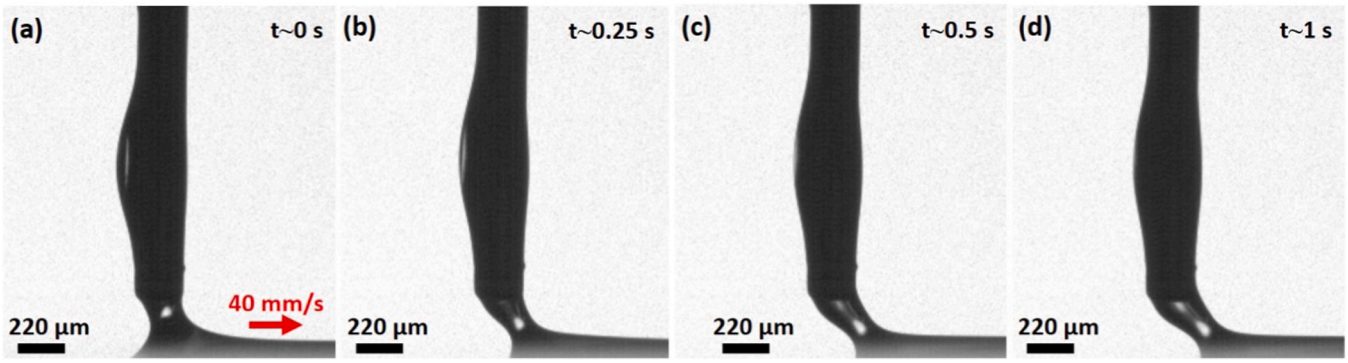


**Fig. 10.** Spot-E extruded at ~ 2 mm/s onto Mylar belt moving at 20 mm/s from 34-gauge needle, 30 psi. (a) t ≈ 0 s (the moment when the E.F. of 2.5 kV/mm was turned off) f. (b) t ≈ 0.25 s (c) t ≈ 0.5 s (d) t ≈ 1 s.

Several woven substrates comprised of both polymer and natural fibers were also tested, to evaluate the benefits of the applied E.F. for printing on varied super-rough surfaces which are traditionally impossible to print ink on using DIW technologies. The surface roughness for the three belts of these types was relatively high. For the polyester (PTA) ribbon, the surface roughness $R_a$ was ~ 200 µm. At 97× magnification, Fig. 11a shows the individual fibers bundled and woven creating a much rougher PTA surface than the Mylar belt seen in Figs. 3–10. Fig. 11b captures a failed print as the ink breaks up into unconnected droplets due to the insufficient wetting on this super-rough substrate. By applying 2.5 kV/mm to the governing electrode, Fig. 11c shows a continuous trace being printed on PTA with an almost zero drag-off distance.

The woven cotton belt is further tested as a substrate. It has an even higher surface roughness with $R_a$ ≈ 360 µm, which is almost impossible to print inks on using the conventional DIW technologies reported in literature. Fig. 12a was taken at 32× magnification, which reveals the overall view of the cotton belt surface patterned by the bundles woven together, while Fig. 12b at 97× magnification demonstrates the individual fibers, which comprise the larger bundles. It should be emphasized that the individual fibers in the woven cotton belt are not necessarily neatly organized within the larger bundles and often leave the confinement of the bundle sometimes reaching several orders of magnitude higher above the printing surface than the average roughness extends. These elevated strands can easily be seen in Fig. 12c and d where the two snapshots, respectively, show a failed printing state without E.F. and a successful intact printing trace with an E.F. strength of 2.5 kV/mm applied.

Another super-rough material was tested as substrate in our study. It was made from bundled jute fibers woven into a ribbon 12.7 mm wide and 2.21 mm thick. The surface roughness based on the bundle diameter was estimated at 1.1 mm and can be observed at 32× and 97× magnifications in Fig. 13a and b, respectively. The woven jute also revealed many individual fibers which are not contained within the bundles, similarly to those observed in Fig. 12b, further decreasing the uniformity of the belt surface used for ink deposition. Once again, a positive effect of the applied electric field on a continuous printed trace line was observed. Fig. 13c shows a failed print without E.F. applied, and Fig. 13d shows a continuous trace successfully printed by our electrostatically-assisted DIW on this roughest substrate, with 2.5 kV/mm E.F. applied to the governing electrode.

### 3.3. Morphology of printed trace line improved by electric field

In the model experimental setup, the E.F. – affected jetting was easily captured via CCD camera due to a stationary nozzle. Upon transitioning to a moving DIW dispensing robot, such a visualization of the extruding ink became too difficult as the nozzle mechanically shifted according to

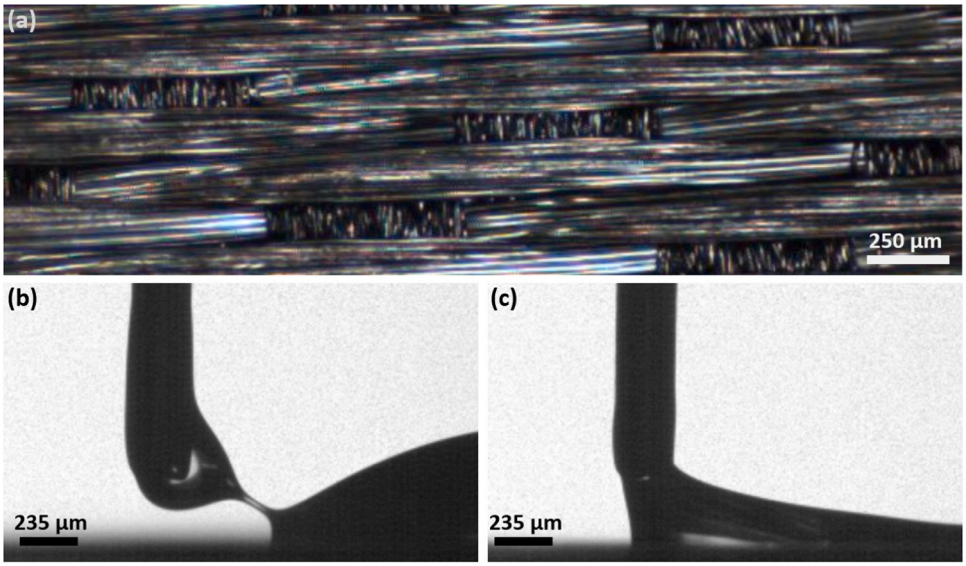


**Fig. 11.** Spot-E extruded at ~ 15 mm/s onto polyester (PTA) belt (0.35 mm thickness) from 32-gauge needle, at the 20 mm/s belt speed, 45 psi. (a) View of bundled fibers at 97× magnification. (b) Failed printing state without E.F. applied. (c) 2.5 kV/mm voltage applied to the governing electrode (out of view in panels b and c).

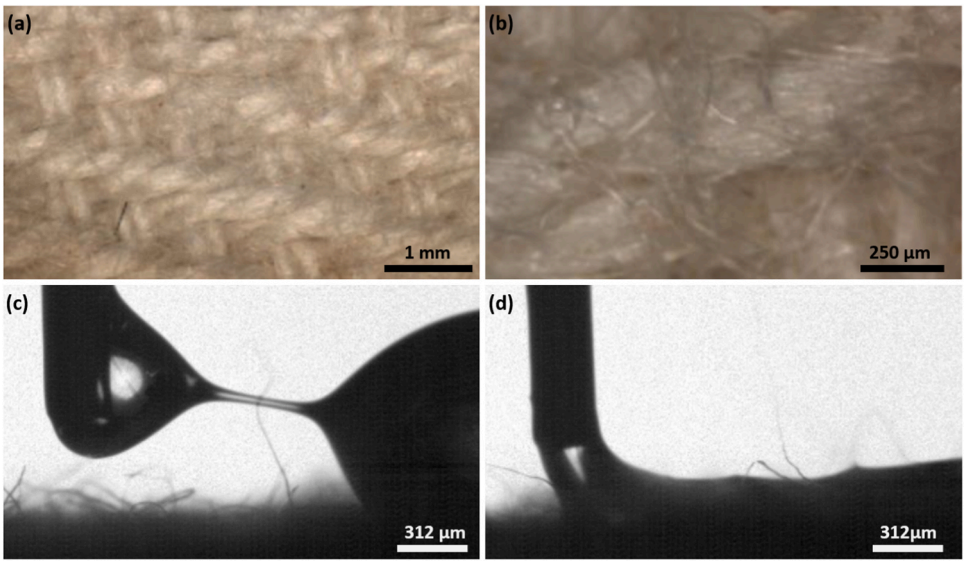


**Fig. 12.** Spot-E extruded at ~ 29 mm/s onto woven cotton belt (0.85 mm thickness) from 30-gauge needle, at the 20 mm/s belt speed, 41 psi. (a)–(b) View of bundled fibers at 32× and 97× magnification, respectively. (c) Failed printing state without E.F. (d) Intact printing line at 2.5 kV/mm voltage applied to the governing electrode which is not in the camera view.

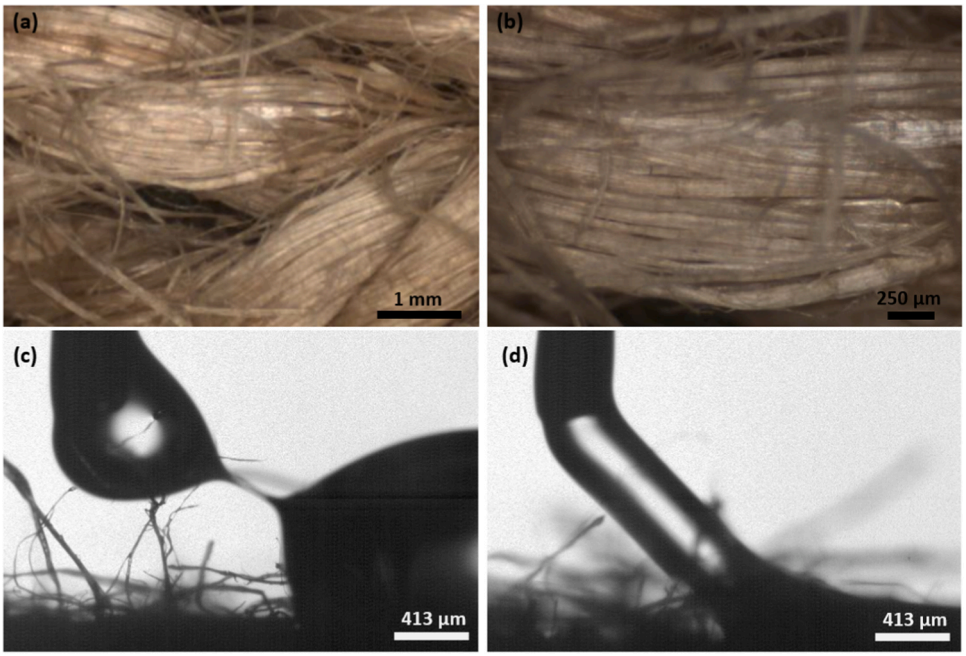


**Fig. 13.** Spot-E extruded at ~ 37 mm/s onto woven jute belt (2.21 mm thickness) from 27-gauge needle, at the 20 mm/s belt speed, 30 psi. (a) View of bundled fibers at 32× magnification. (b) View of bundled fibers at 97× magnification. (c) Failed printing state without E.F. applied. (d) Successful intact trace resulting from 2.5 kV/mm applied to the governing electrode which is not in the camera view.

the printing program. While the pixelated data of the advancing lamella was not recorded during prints conducted with the DIW robot, an achievable increased printing speed and versatility facilitated by the electrically-modified needle can clearly be observed in the printed traces after completion. Fig. 14 shows four of the ten results of Spot-E printed at different translating velocities as 10 cm trace lines onto a glass sheet 1 mm in thickness. For the ten printing cases, the printing speed was increased in 50 mm/s increments in the 50–500 mm/s range. Fig. 14 compares, as an example, four of the ten printing speeds sub-divided into those printed without E.F. (panels denoted by the lower-case letters) and with the applied E.F. (panels denoted with the upper-case letters). For example, the trace in Fig. 14a is printed at 50 mm/s with no E.F., while the one shown in Fig. 14A is printed at 50 mm/s with 2.5 kV/mm E.F. applied to the governing electrode. The printing speed in Fig. 14 is in the 50–500 mm/s range and increase in 150 mm/s increments from panel (a) to panel (b) and so on until the maximum velocity (500 mm/s) of the DIW robot is reached. When analyzing the different trace morphologies in the lower-case letter panels in Fig. 14 without E.F. applied, one can see that only the first printing speed (50 mm/s) resulted in a continuous trace line. It should be emphasized that of the total of ten velocities, the first two (50 and 100 mm/s) resulted in continuous trace lines. Of the two continuous trace lines printed in the absence of the E.F. only Fig. 14a (for the lowest printing speed) reveals a relatively uniform trace width. Even an increase in the

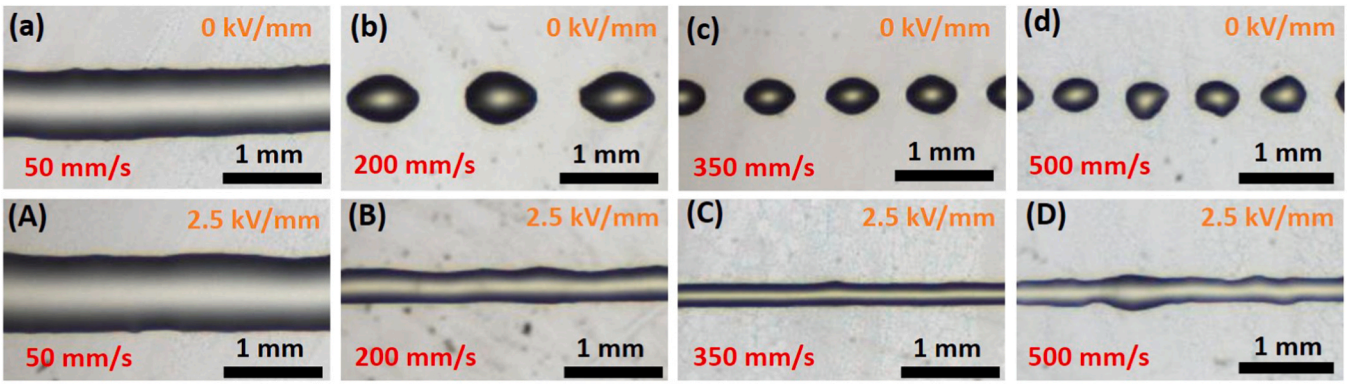


**Fig. 14.** Spot-E extruded at ~ 10 mm/s onto glass substrate (1 mm thickness) from 32-gauge needle at 30 psi. Printed on the DIW machine. (a) 50 mm/s, 0 kV/mm. (A) 50 mm/s, 2.5 kV/mm. (b) 200 mm/s, 0 kV/mm. (B) 200 mm/s, 2.5 kV/mm. (c) 350 mm/s, 0 kV/mm. (C) 350 mm/s, 2.5 kV/mm. (d) 500 mm/s, 0 kV/mm. (D) 500 mm/s, 2.5 kV/mm.

printing speed up to 100 mm/s revealed significant undulations (bulging). Bulging of this magnitude can also be considered a defect in DIW. These types of defects continued to escalate at higher printing speeds resulting in eight discontinuous prints at every printing speed higher than 100 mm/s, with several being shown in Fig. 14. It should be emphasized that while 50 mm/s is considered adequate for DIW printing, the appropriate speed is judged based on the corresponding resolution and cost. The upper-case letter panels in Fig. 14 reveal that the 2.5 kV/mm voltage applied to the governing electrode facilitates printing intact trace lines up to the machine's maximum-capability speed of 500 mm/s. Of the ten distinct printing speeds tested, in 90% of the cases with applied E.F. intact 10 cm-long printed traces were obtained. An anomaly can be seen in Fig. 15a were even with the E.F. applied, a small portion of the trace was discontinuous. This is likely due to an uncontrollable nuisance variable unable to be factored out with blocking between print speeds and randomization of runs, e.g., harmonic vibrations or instabilities.

As previously mentioned, even though the electric potential applied to the governing electrode revealed a significant increase in the printing speeds of trace lines, the results were not always perfect. Fig. 15a highlights a random break in the trace line printed at 200 mm/s with the applied E.F., albeit the majority of the printed traces at these speeds were continuous. In the aforementioned experiments, the E.F. pulls the triple line of the jetted ink's footprint in the direction of printing with an electric field strength of ~ 2.5 kV/mm. However, increasing the E.F. strength close to or above the dielectric breakdown of air (i.e., 3 kV/mm) resulted in the completely discontinuous patterns shown in Fig. 15b printed at 3 kV/mm. This phenomenon is likely caused by the electrically-driven instability of the trace, which becomes dominant in comparison to the previously discussed electrowetting pulling of the triple line.

Below the 3 kV/mm threshold, an additional experiment was performed using the DIW robot and printing onto woven cotton substrate previously tested in the model belt drive setup of Fig. 2. The results in Fig. 16 show the top views of Spot-E traces extruded through a 30-gauge needle at 41 psi with a translating print velocity of 40 mm/s along the x-axis with the other two print axes fixed. Fig. 16a shows the discontinuous trace line printed without E.F., whereas Fig. 16b shows the continuous line printed with the E.F. of 2.5 kV/mm applied to the governing electrode. Fig. 16c shows the continuous trace which could be printed at a doubled print velocity (80 mm/s) with the E.F. of 2.5 kV/mm applied. It is seen that doubling the print velocity did not disrupt the trace line but rather diminished its width to one half of that seen in Fig. 16b.

## 4. Theory of DIW without and with the electric field and comparison with the experimental data

### 4.1. Jet configuration without electric field applied

Here we aim at the theoretical description of the jet configuration in the DIW process and its modification by the electric forces. For a steady-state jet, the governing equations read [32]

$$\frac{dfV_\tau}{d\xi} = 0 \tag{1}$$

$$\frac{d}{d\xi}(P\boldsymbol{\tau} + \mathbf{Q}) = 0 \tag{2}$$

$$\frac{d\mathbf{M}}{d\xi} + \boldsymbol{\tau} \times \mathbf{Q} = 0 \tag{3}$$

Eq. (1) is the continuity equation which expresses the mass balance, with f being the cross-sectional area of the jet, $V_\tau$ being the velocity magnitude (the velocity projection to the jet axis with the local unit vector $\boldsymbol{\tau}$; cf. Fig. 17), and $\xi$ being the arc length. Eq. (2) is the force balance (the momentum balance equation in the inertialess approximation valid for slowly moving viscous jets of interest here), with P being the magnitude of the local longitudinal force in the jet cross-section, and $\mathbf{Q}$ being the local shearing force in the jet cross-section. Eq. (3) is the moment-of-momentum equation, with $\mathbf{M}$ being the local moment of stresses acting in the jet cross-section. In Eqs. (1)–(3) and

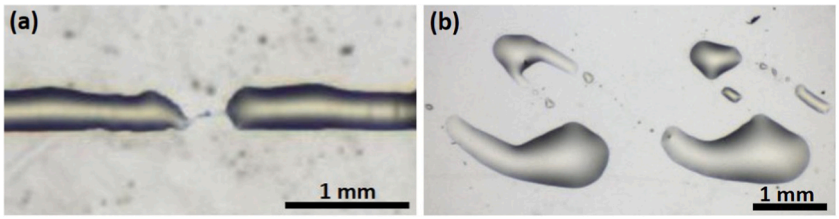


**Fig. 15.** Spot-E extruded onto glass substrate (1 mm thickness) from 32-gauge needle at ~ 10 mm/s with 2.5 kV/mm applied to the governing electrode, 30 psi. (a) Short break in the trace line printed at 200 mm/s. (b) Electrically-driven instability of printed traces at elevated E.F. strength of 3.0 kV/mm.


**Fig. 16.** Spot-E extruded at ~ 29 mm/s from 30-gauge needle onto woven cotton (0.85 mm thickness) adhered with double-sided tape to a glass substrate (1 mm thickness). (a) 0 kV/mm, 40 mm/s, discontinuous trace ~ 3.5 mm wide. (b) 2.5 kV/mm, 40 mm/s, continuous trace ~ 2 mm wide. (c) 2.5 kV/mm, 80 mm/s, continuous trace ~ 1 mm wide.

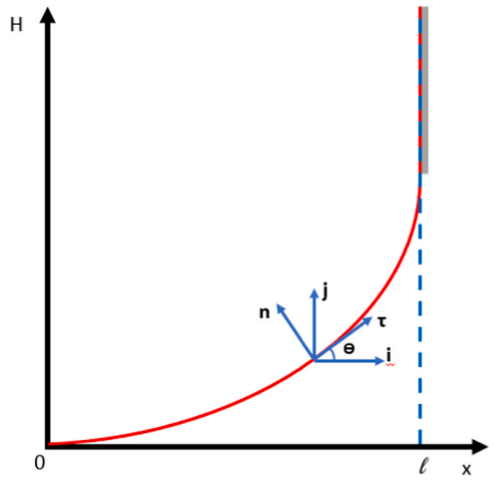


**Fig. 17.** Sketch of the jet axis shown in red, with the coordinate axes and unit vectors used. The belt here moves vertically at $x = \ell$. (For interpretation of the references to color in this figure legend, the reader is referred to the web version of this article.)

hereinafter the boldfaced characters denote vectors.

In the present case the jet axis is a plane curve. Accordingly, **Q** has the only non-zero component in the direction of the unit normal vector to the jet axis **n**, i.e. $\mathbf{Q} = \mathbf{n}Q_n$, and **M** has the only non-zero component in the direction of the unit binormal vector to the jet axis **b**, i.e. $\mathbf{M} = \mathbf{b}M_b$; cf. Fig. 17. Then, Eq. (3) takes the following form

$$\frac{dM_b}{d\xi} + Q_n = 0 \tag{4}$$

where according to [32]

$$M_b = 3\mu I\left(\frac{dkV_\tau}{d\xi} - \frac{3}{2}k\frac{dV_\tau}{d\xi}\right) \tag{5}$$

with μ being the liquid viscosity, I being the moment of inertia of the jet cross-section, and k being the curvature of the jet axis.

Using Eqs. (4) and (5), one finds the shearing force as

$$Q_n = -3\mu\frac{d}{d\xi}\left[I\left(\frac{dkV_\tau}{d\xi} - \frac{3}{2}k\frac{dV_\tau}{d\xi}\right)\right] \tag{6}$$

Note also that jet cross-section in bending stays practically circular [32] and thus,

$$f = \pi a^2, \quad I = \frac{\pi a^4}{4} \tag{7}$$

where a is the local cross-sectional radius.

It should be emphasized that in Eqs. (2) and (3) we disregard the gravity force assuming its effect to be negligibly small for DIW jets. Also, here the unmodified DIW process is considered first, i.e., the effect of the electric forces will be included separately.

Using the Frenet–Serret formulae, transform Eq. (2) to the following form

$$\boldsymbol{\tau}\frac{dP}{d\xi} + Pk\mathbf{n} + \mathbf{n}\frac{dQ_n}{d\xi} - kQ_n\boldsymbol{\tau} = 0 \tag{8}$$

In the projection of Eq. (8) to the tangent, the term $-kQ_n\boldsymbol{\tau}$ can be neglected compared to $\boldsymbol{\tau}dP/d\xi$. Then, the tangential projection of Eq. (8)

reads

$$\frac{dP}{d\xi} = 0 \tag{9}$$

According to Yarin [32], the longitudinal force is given by

$$P = 3\mu f \frac{dV_\tau}{d\xi} \tag{10}$$

Integration Eqs. (1) and (2), one finds

$$fV_\tau = q, \quad 3\mu f \frac{dV_\tau}{d\xi} = F \tag{11}$$

where the constants of integration q and F have the meaning of the given volumetric flow rate in the jet q, and the still unknown pulling force imposed on the jet by the belt F.

Excluding f from Eq. (11), one obtains the differential equation for $V_\tau$

$$\frac{3\mu}{V_\tau}\frac{dV_\tau}{d\xi} = \frac{F}{q} \tag{12}$$

Integrating the later and using the boundary condition on the nozzle exit

$$\xi = 0, \quad V_\tau = V_{\tau 0} \tag{13}$$

where $V_{\tau 0}$ is the jet velocity at the nozzle exit, which is known, one obtains the velocity distribution along the jet

$$V_\tau = V_{\tau 0}\exp\left(\frac{F}{3\mu q}\xi\right) \tag{14}$$

The velocity of the jet on the belt at $\xi = L$ (where L is the total jet length from the nozzle to the belt) $V_{\tau 1}$ is also known, albeit L is still unknown. Accordingly, Eq. (14) yields the following relation of the unknown force F to the unknown length L

$$F = \frac{3\mu q}{L}\ln\left(\frac{V_{\tau 1}}{V_{\tau 0}}\right) \tag{15}$$

The normal projection of Eq. (8) reads

$$Pk + \frac{dQ_n}{d\xi} = 0 \tag{16}$$

Substituting the expression for the shearing force (6) and using Eqs. (10) and (11) for the longitudinal force, transform Eq. (16) to the following form

$$Fk - 3\mu\frac{d^2}{d\xi^2}\left[I\left(\frac{dkV_\tau}{d\xi} - \frac{3}{2}k\frac{dV_\tau}{d\xi}\right)\right] = 0 \tag{17}$$

Denote by θ the angle between the jet axis and the axis Ox directed from the nozzle normally to the belt. Then, the curvature of the jet axis can be expressed as

$$k = \frac{d\theta}{d\xi} \tag{18}$$

and Eq. (17) takes the following form

$$F\frac{d\theta}{d\xi} - 3\mu\frac{d^2}{d\xi^2}\left\{I\left[\frac{d}{d\xi}\left(\frac{d\theta}{d\xi}V_\tau\right) - \frac{3}{2}\frac{d\theta}{d\xi}\frac{dV_\tau}{d\xi}\right]\right\} = 0 \tag{19}$$

The solution of this fourth-order differential equation for θ is subjected to the following for boundary conditions

$$\xi = 0, \quad \theta = 0 \tag{20}$$

$$\xi = 0, \quad \frac{d}{d\xi}\left\{I\left[\frac{d}{d\xi}\left(\frac{d\theta}{d\xi}V_\tau\right) - \frac{3}{2}\frac{d\theta}{d\xi}\frac{dV_\tau}{d\xi}\right]\right\} = 0 \tag{21}$$

$$\xi = L, \quad \theta = \frac{\pi}{2} \tag{22}$$

$$\xi = L, \quad \frac{d\theta}{d\xi} \to \infty \tag{23}$$

The condition (20) implies that the jet is coaxial to the nozzle when it leaves it; the condition (21) means that the shearing force $Q_n = 0$ at the nozzle exit; the conditions (22) and (23) correspond to the jet roll-over the moving belt.

Even though the relation of F to L is known from Eq. (15), it should be emphasized that the problem formed by the fourth order differential equation (19) with the four boundary conditions (20)–(23) still contains one unknown – the total jet length L. Accordingly, an additional integral condition is required, namely,

$$\ell = \int_0^L \cos[\theta(\xi)]d\xi \tag{24}$$

where $\ell$ is the given distance from the nozzle to the belt along the x-axis, i.e., the standoff distance.

After finding $\theta = \theta(\xi)$, the shape of the jet $H = H(x)$ is found using the following geometric relations

$$H(\xi) = \int_0^\xi \sin[\theta(\xi)]d\xi \tag{25}$$

$$x = \int_0^\xi \cos[\theta(\xi)]d\xi \tag{26}$$

Eq. (19) with the boundary conditions (20) and (21) admits the following integration

$$F\theta - 3\mu\frac{d}{d\xi}\left\{I\left[\frac{d}{d\xi}\left(\frac{d\theta}{d\xi}V_\tau\right) - \frac{3}{2}\frac{d\theta}{d\xi}\frac{dV_\tau}{d\xi}\right]\right\} = 0 \tag{27}$$

Additionally, the second Eq. (7) and the first Eq. (11) yield

$$I = \frac{q^2}{4\pi}\frac{1}{V_\tau^2} \tag{28}$$

Then, using Eqs. (14) and (28), transform Eq. (27) to the following dimensionless form

$$\frac{\ln \overline{V_{\tau 1}}}{\overline{L}}\theta - \frac{\overline{a_0}^2}{4}\frac{d}{d\xi}\left[\overline{V_{\tau 1}}^{-\xi/\overline{L}}\left(\frac{d^2\theta}{d\xi^2} - \frac{\ln \overline{V_{\tau 1}}}{2\overline{L}}\frac{d\theta}{d\xi}\right)\right] = 0 \tag{29}$$

where ξ is rendered dimensionless by $\ell$, and – in transition – $V_\tau$ and F were rendered dimensionless by $V_{\tau 0}$ and $\mu q/\ell$, respectively.

Eq. (29) involves three dimensionless groups

$$\overline{V_{\tau 1}} = \frac{V_{\tau 1}}{V_{\tau 0}}, \quad \overline{a_0} = \frac{a_0}{\ell}, \quad \overline{L} = \frac{L}{\ell} \tag{30}$$

of which the first two are given, whereas the third one is found as discussed above.

The boundary conditions (20)–(23) take the following dimensionless form

$$\xi = 0, \quad \theta = 0 \tag{31}$$

$$\xi = 0, \quad \frac{d}{d\xi}\left[\overline{V_{\tau 1}}^{-\xi/\overline{L}}\left(\frac{d^2\theta}{d\xi^2} - \frac{\ln \overline{V_{\tau 1}}}{2\overline{L}}\frac{d\theta}{d\xi}\right)\right] = 0 \tag{32}$$

$$\xi = \overline{L}, \quad \theta = \frac{\pi}{2} \tag{33}$$

$$\xi = \overline{L}, \quad \frac{d\theta}{d\xi} \to \infty \tag{34}$$

Note that one of the two conditions (31) and (32) is already redundant, because of Eq. (29).

In addition, the condition (24) takes the form

$$1 = \int_0^{\bar{L}} \cos[\theta(\xi)]d\xi \tag{35}$$

Eqs. (25) and (26) do not change their form when x, H and ξ are rendered dimensionless by $\ell$.

Consider the realistic case of $\overline{V_{\tau 1}} >> 1$. It is easy to see that one expects to find a solution, in which

$$\frac{d^3\theta}{d\xi^3} >> \frac{\ln \overline{V_{\tau 1}}}{2\bar{L}} \frac{d^2\theta}{d\xi^2} >> \frac{\ln \overline{V_{\tau 1}}}{2\bar{L}} \frac{d\theta}{d\xi} \tag{36}$$

These inequalities will be assumed to hold now, and proven a posteriori.

Implying the inequalities (36), the problem (29), (31)–(34) is recast as

$$\frac{d^3\theta}{d\xi^3} + \kappa \overline{V_{\tau 1}}^{\xi/\bar{L}} \theta = 0 \tag{37}$$

$$\xi = 0, \quad \theta = \frac{d^3\theta}{d\xi^3} = 0 \tag{38}$$

$$\xi = \bar{L}, \quad \theta = \frac{\pi}{2}, \quad \frac{d\theta}{d\xi} \to \infty \tag{39}$$

In Eq. (37) the following notation is used

$$\kappa = -\frac{4}{\bar{a}_0^2} \frac{\ln \overline{V_{\tau 1}}}{\bar{L}} \tag{40}$$

Note once again, that one of the two conditions (38) is redundant, because of Eq. (37).

In the case of $\overline{V_{\tau 1}} >> 1$ formation of the boundary layer near $\xi = \bar{L}$ is expected. In this boundary layer Eq. (37) takes the form

$$\varepsilon \frac{d^3\theta}{d\xi^3} + \kappa\theta = 0 \tag{41}$$

where

$$\varepsilon = \frac{1}{\overline{V_{\tau 1}}} << 1 \tag{42}$$

As usual in the matched asymptotic expansions of the boundary layer theory [33,34], the inner stretched coordinate is introduces as

$$X = \frac{\bar{L} - \xi}{\varepsilon^{1/3}} \tag{43}$$

Then, Eq. (41) takes the following asymptotic form

$$\frac{d^3\theta}{dX^3} + |\kappa|\theta = 0 \tag{44}$$

Its solution reads

$$\theta = C_1 e^{-\gamma X} + e^{\gamma X}\left(C_2 \cos\frac{\sqrt{3}}{2}\gamma X + C_3 \sin\frac{\sqrt{3}}{2}\gamma X\right) \tag{45}$$

where $C_1$–$C_3$ are the constants of integration and $\gamma = |\kappa|^{1/3}$.

The inner solution (45) is supposed to be matched with the outer solution outside the boundary layer (still to be found) as $X \to \infty$. That means that $C_2 = C_3 = 0$. On the other hand, the first boundary condition (39) yields $C_1 = \pi/2$, and thus, in the boundary layer $\theta = (\pi/2)\exp(-\gamma X)$, i.e.,

$$\theta = \frac{\pi}{2}\exp\left[-\left(\frac{4}{\bar{a}_0^2}\frac{\ln \overline{V_{\tau 1}}}{\bar{L}}\right)^{1/3}\left(\bar{L} - \xi\right)\right] \tag{46}$$

It is easy to see that for $\varepsilon << 1$, the second boundary condition (39) holds, because $d\theta/d\xi \sim \varepsilon^{-1/3} \to \infty$. Moreover, for $\varepsilon << 1$, $d^2\theta/d\xi^2 \sim \varepsilon^{-2/3}$, $d^3\theta/d\xi^3 \sim \varepsilon$, which proves the inequalities (36).

Outside the boundary layer, Eq. (37) becomes

$$\frac{d^3\theta}{d\xi^3} + \kappa\theta = 0 \tag{47}$$

Its solution is given by Eq. (45) with ξ instead of X. To satisfy the outer boundary conditions (38) and achieve matching with the inner solution (46) as $\xi \to \bar{L}$, all the constants of integration should be zero, and thus, the outer solution becomes

$$\theta = 0 \tag{48}$$

In the boundary layer when ξ is very close to $\bar{L}$, the inner solution $\theta = (\pi/2)\exp(-\gamma X)$ can be approximated by its truncated expansion in the Taylor series, $\theta \approx (\pi/2)(1 - \gamma X)$, which, together with the outer solution (48), allows one to evaluate the integrals in Eqs. (35), (25) and (26), to find

$$\bar{L} \approx 1 + \left(\frac{4-\pi}{4}\right)\left(\frac{\bar{a}_0^2}{4}\frac{1}{\ln \overline{V_{\tau 1}}}\frac{1}{\overline{V_{\tau 1}}}\right)^{1/3} \tag{49}$$

and the jet axis H = H(x) in the parametric form (with ξ being the parameter) as

$$x(\xi) = \begin{cases} \xi, & for \ \ 0 \le \xi < \xi_0, \\ \xi_0 + \dfrac{\pi}{2}\left(\dfrac{4}{\bar{a}_0^2}\overline{V_{\tau 1}} \ln \overline{V_{\tau 1}}\right)^{1/3}\left(\bar{L}\xi - \dfrac{\xi^2}{2} - \bar{L}\xi_0 + \dfrac{\xi_0^2}{2}\right), & for \ \ \xi_0 \le \xi \le \bar{L} \end{cases} \tag{51}$$

Note that in Eqs. (50) and (51) the outer boundary of the boundary layer is taken at $\xi_0 = \bar{L} - O(\varepsilon^{1/3})$, in particular, at

$$\xi_0 = 1 - \frac{\pi}{4}\left(\frac{\bar{a}_0^2}{4}\frac{1}{\overline{V_{\tau 1}} \ln \overline{V_{\tau 1}}}\right)^{1/3} \tag{52}$$

Eq. (52) also yields the lateral coordinate at which the deflected jet meets the moving belt

$$H\left(\bar{L}\right) = \frac{(1 - \pi^2/24)}{\left[\left(4/\bar{a}_0^2\right)\overline{V_{\tau 1}} \ln \overline{V_{\tau 1}}\right]^{1/3}} \tag{53}$$

Fig. 18a illustrates the predicted jet configuration near the deflecting belt in the boundary layer, i.e., the one given by Eq. (46). The

$$H(\xi) = \begin{cases} 0, & for \ \ 0 \le \xi < \xi_0, \\ \xi - \xi_0 + \dfrac{\pi^2}{24}\left(\dfrac{4}{\bar{a}_0^2}\overline{V_{\tau 1}} \ln \overline{V_{\tau 1}}\right)^{2/3}\left[\left(\bar{L} - \xi\right)^3 - \left(\bar{L} - \xi_0\right)^3\right], & for \ \ \xi_0 \le \xi \le \bar{L} \end{cases} \tag{50}$$

corresponding jet configuration given by Eqs. (50)–(52) in this case is shown in Fig. 18b.

### 4.2. Jet configuration affected by the applied electric field

Consider the effect of the electric forces on jet configuration. Let the jet has a net charge $e_0$ per unit length when it is issued from the nozzle. Material elements in the jet are stretched and the length of a unit element becomes equal to $\lambda = \sqrt{1+(dH/dx)^2} = 1/\cos\theta$ because $dH/dx = \tan\theta$ and in the present case $\cos\theta > 0$ because $-\pi/2 \le \theta \le \pi/2$. Accordingly, the charge conservation in a material jet element means that the current charge per unit length is $e = e_0/\lambda = e_0\cos\theta$.

Assume that in the space surrounding the jet an electric field is imposed by an electrode system. In particular, consider the electric field strength **E** parallel to the belt and directed opposite to the direction of the belt motion, i.e., $\mathbf{E} = -E\mathbf{j}$, where E is the magnitude and **j** is the unit vector of the H-axis, i.e. of the direction of the belt motion. According to Fig. 17, $\mathbf{j} = \mathbf{n}\cos\theta + \boldsymbol{\tau}\sin\theta$, and thus, the electric force acting on a unit element of the jet $\mathbf{F}_{el} = e\mathbf{E}$ is given by the following expression

$$\mathbf{F}_{el} = -e_0 E\cos\theta(\mathbf{n}\cos\theta + \boldsymbol{\tau}\sin\theta) \tag{54}$$

Accounting for this force in the governing equations, yields the following system of equations generalizing Eqs. (1)–(3) for the case where the electric force is present [32]

$$\frac{dfV_\tau}{d\xi} = 0 \tag{55}$$

$$\frac{d}{d\xi}(P\boldsymbol{\tau} + \mathbf{Q}) + \mathbf{F}_{el} = 0 \tag{56}$$

$$\frac{d\mathbf{M}}{d\xi} + \boldsymbol{\tau}\times\mathbf{Q} - I\mathbf{n}\times\mathbf{F}_{el} = 0 \tag{57}$$

As before, the only non-zero projection of Eq. (57) is the one on the binormal **b**, and it reads [cf. with Eq. (4)]

$$\frac{dM_b}{d\xi} + Q_n - e_0 EI\cos\theta\sin\theta = 0 \tag{58}$$

Using the Frenet–Serret formulae, transform Eq. (56) to the following form

$$\boldsymbol{\tau}\frac{dP}{d\xi} + Pk\mathbf{n} + \mathbf{n}\frac{dQ_n}{d\xi} - kQ_n\boldsymbol{\tau} - e_0 E\cos\theta(\mathbf{n}\cos\theta + \boldsymbol{\tau}\sin\theta) = 0 \tag{59}$$

As in Section 4.1, the realistic case of $\overline{V_{\tau 1}} >> 1$ is in focus when the appearance of the boundary layer in the jet configuration near the belt is expected. The extra term on the left in Eq. (58) [cf. with Eq. (4)] is negligibly small in the boundary layer near the belt where $\theta \to \pi/2$. Due to the same reason, the effect of the electric force in Eq. (59) in the boundary layer is negligibly small, and the entire solution in the boundary layer found in the previous Section 4.1, Eqs. (50) and (51), holds with a minor modification

$$x(\xi) = \begin{cases} \xi, & for\ \ 0 \le \xi < \xi_0, \\ \xi_0 + \dfrac{\pi}{2}\left(\dfrac{4}{\overline{a}_0^2}\overline{V_{\tau 1}}\ln\overline{V_{\tau 1}}\right)^{1/3}\left(\overline{L}\xi - \dfrac{\xi^2}{2} - \overline{L}\xi_0 + \dfrac{\xi_0^2}{2}\right), & for\ \ \xi_0 \le \xi \le \overline{L} \end{cases} \tag{61}$$

Namely, in the boundary layer at $\xi_0 \le \xi \le \overline{L}$ the matching of H in Eq. (60) brings in an extra term $H(\xi_0)$ because the outer solution is affected now by the electric field, and $H(\xi_0) \ne 0$ anymore. Note that in Eqs. (60) and (61) the previous expression for $\overline{L}$ given by Eq. (49) is used as a reasonable approximation having in mind that the main contribution in the integral of Eq. (35) is associated with the boundary layer domain. Outside the boundary layer where θ is close to zero the only significant contribution of the electric field is in the normal component of Eq. (59), which rakes the following dimensionless form

$$\frac{\ln\overline{V_{\tau 1}}}{\overline{L}}\frac{d\theta}{d\xi} - \frac{\overline{a}_0^2}{4}\frac{d^2}{d\xi^2}\left[\overline{V_{\tau 1}}^{-\xi/\overline{L}}\left(\frac{d^2\theta}{d\xi^2} - \frac{\ln\overline{V_{\tau 1}}}{2\overline{L}}\frac{d\theta}{d\xi}\right)\right] = \overline{E}\cos^2\theta \tag{62}$$

where a new dimensionless group, the dimensionless electric field strength, appears

$$\overline{E} = \frac{e_0 E\ell^2}{\mu q} \tag{63}$$

Having in mind the inequalities (36) and the fact than in the outer solution θ is close to zero, and thus, $\cos^2\theta \approx 1$, transform Eq. (62) to the following one

$$\frac{d^4\theta}{d\xi^4} + \omega\frac{d\theta}{d\xi} = -\frac{4}{\overline{a}_0^2}\overline{E} \tag{64}$$

where

$$\omega = -\frac{4}{\overline{a}_0^2}\ln\overline{V_{\tau 1}} \tag{65}$$

Integrating Eq. (64) once and using the boundary conditions (38), we obtain

$$\frac{d^3\theta}{d\xi^3} + \omega\theta = -\frac{4}{\overline{a}_0^2}\overline{E}\xi \tag{66}$$

The solution of the latter equation reads

$$\theta = C_1 e^{-\gamma\xi} + e^{\gamma\xi}\left(C_2\cos\frac{\sqrt{3}}{2}\gamma\xi + C_3\sin\frac{\sqrt{3}}{2}\gamma\xi\right) - \frac{4}{\overline{a}_0^2\omega}\overline{E}\xi \tag{67}$$

where $C_1$–$C_3$ are the constants of integration and $\gamma = \omega^{1/3}$. Note that $\gamma < 0$ because $\omega < 0$.

Applying to Eq. (67) the boundary conditions (38) and the matching condition

$$\xi \to \xi_0, \quad \theta \to 0 \tag{68}$$

One finds the constants $C_1$–$C_3$ as

$$H(\xi) = \begin{cases} 0, & for\ \ 0 \le \xi < \xi_0, \\ H(\xi_0) + \xi - \xi_0 + \dfrac{\pi^2}{24}\left(\dfrac{4}{\overline{a}_0^2}\overline{V_{\tau 1}}\ln\overline{V_{\tau 1}}\right)^{2/3}\left[\left(\overline{L} - \xi\right)^3 - \left(\overline{L} - \xi_0\right)^3\right], & for\ \ \xi_0 \le \xi \le \overline{L} \end{cases} \tag{60}$$

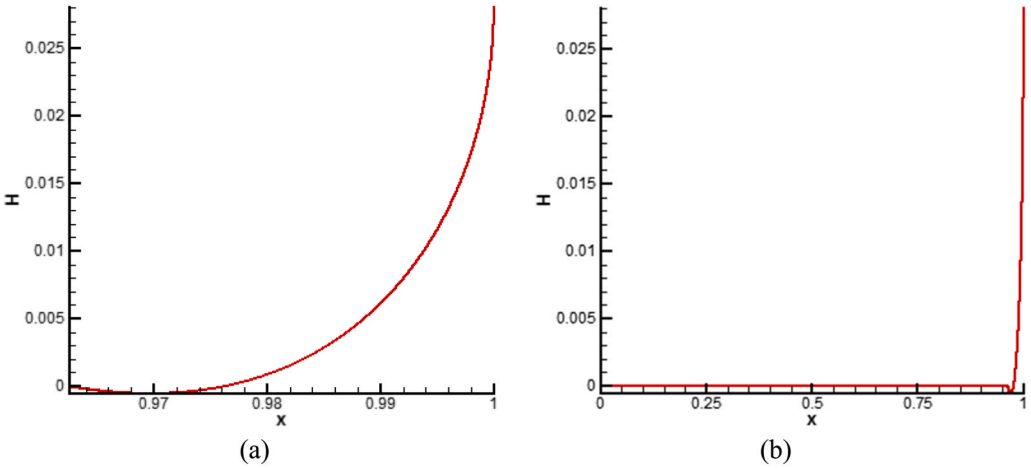


**Fig. 18.** (a) The predicted jet configuration in the boundary layer near the deflecting belt moving in the direction of the H axis. The parameter values: $\overline{a_0} = 0.1$, and $\overline{V_{\tau 1}} = 10$. No E.F. is applied. (b) The predicted overall jet configuration. The parameter values: $\overline{a_0} = 0.1$, and $\overline{V_{\tau 1}} = 10$. No E.F. is applied.

$$C_1 = \frac{\left(4/\overline{a_0}^2\omega\right)\overline{E}\xi_0}{\exp(-\gamma\xi_0) - \exp(\gamma\xi_0)\left[\cos\sqrt{3}\gamma\xi_0/2 + \left(2/3^{5/2}\right)\sin\sqrt{3}\gamma\xi_0/2\right]} \tag{69}$$

$$C_2 = -C_1, \quad C_3 = -\frac{2}{3^{5/2}}C_1 \tag{70}$$

The configuration of the jet affected by the electric field corresponding to the outer solution (67), (69) and (70) is found by the numerical integration of the following equations at $0 \le \xi \le \xi_0$

$$\frac{dH}{d\xi} = \sin[\theta(\xi)], \quad \frac{dx}{d\xi} = \cos[\theta(\xi)] \tag{71}$$

subjected to the following boundary conditions

$$\xi = 0, \quad H = 0, \quad x = 0 \tag{72}$$

This integration, in particular, allows one to find $H(\xi_0)$ required in Eq. (60). The latter also yields the value of the deflection of the jet on the belt as

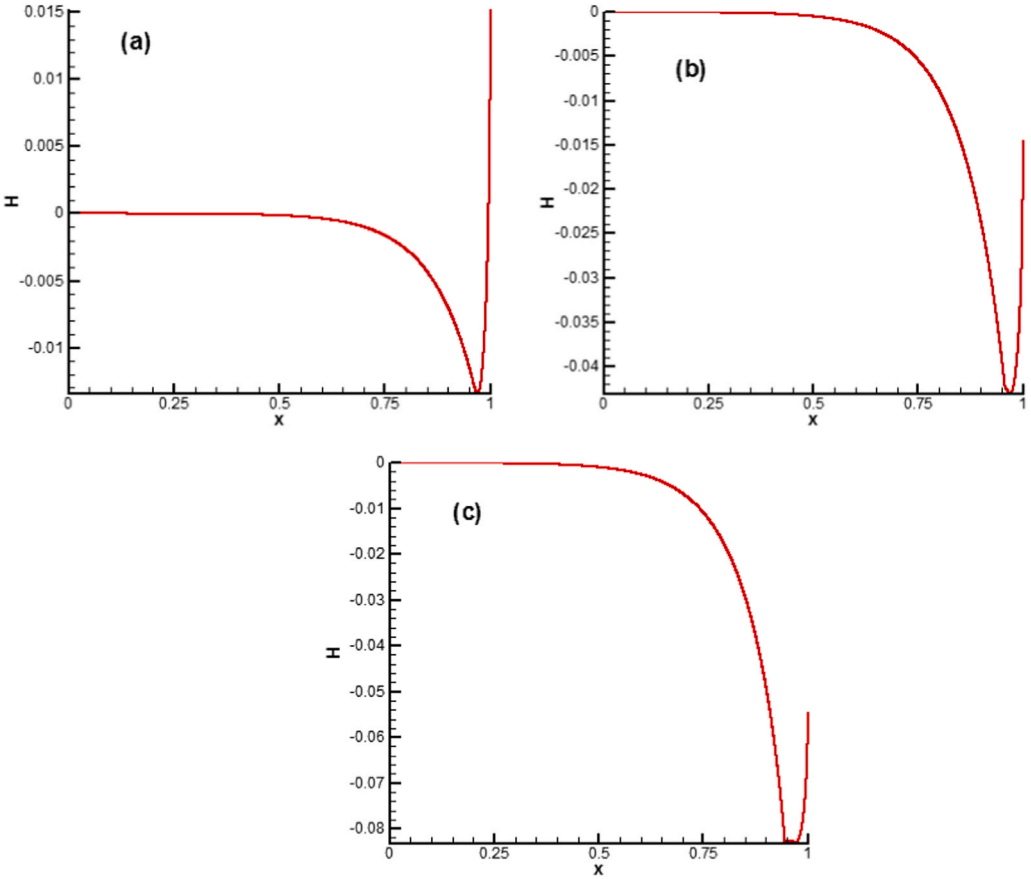


**Fig. 19.** The predicted overall jet configurations affected by the E.F. The parameter values: $\overline{a_0} = 0.1$, and $\overline{V_{\tau 1}} = 10$ **. (a)** $\overline{E} = 0.3$, **(b)** $\overline{E} = 1$, **(c)** $\overline{E} = 2$.

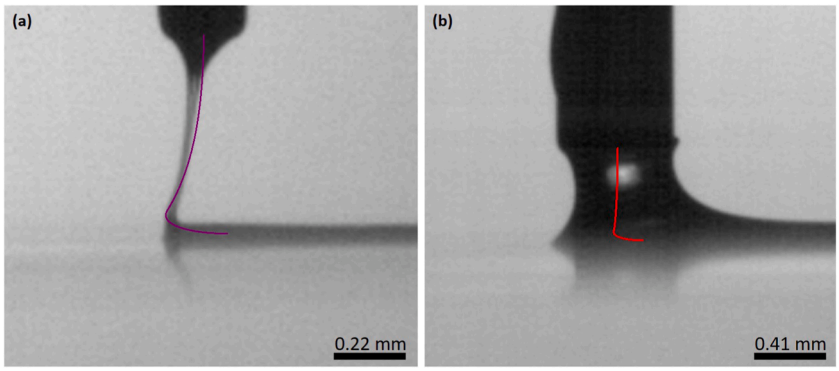


**Fig. 20.** Jet of Spot-E deposited on the belt moving horizontally to the right with the E.F. pulling the jet in the opposite direction. The colored lines show the theoretically predicted centerlines. The dimensionless E.F. strength values used in the theoretical predictions are: (a) $\overline{E} = 0.5$ (purple line) (b) $\overline{E} = 0.1$ (red line). (For interpretation of the references to color in this figure legend, the reader is referred to the web version of this article.)

$$H\left(\overline{L}\right) = H(\xi_0) + \frac{(1-\pi^2/24)}{\left[\left(4/\overline{a}_0^2\right)\overline{V}_{\tau 1}\ln\overline{V}_{\tau 1}\right]^{1/3}} \tag{73}$$

which modifies Eq. (53) in the case when the effect of the electric field is important.

The predicted jet configurations affected by the applied electric field are illustrated in Fig. 19.

The results in Fig. 19 show how the progressively stronger electric field more and more pulls the jet against the direction of the belt motion, essentially diminishing the drag-off distance. It is also instructive to compare these results with the jet configuration predicted without the electric field in Fig. 18.

### 4.3. Theoretical predictions versus the experimental data

In the experiments Spot-E of viscosity of 0.3 Pa s was extruded through a needle of the inner cross-sectional radius $a_0 = 0.207$ mm, of length of 25.4 mm, at the pressure drop of 68948 Pa. The distance between the nozzle exit and the belt was $\ell = 0.333$ *mm*. Using the Poiseuille law, the average velocity $V_{\tau 0} = 3.21$ mm/s, which, indeed, corresponds to laminar flow, as implied. Accordingly, in the case of the belt velocity of $V_{\tau 1} = 40$ mm/s, in the absence of the electric field the values of the relevant dimensionless parameters are the following: $\overline{a_0} = 0.622$, $\overline{V_{\tau 1}} = 12.46$, and $\overline{E} = 0$. For the specific case of $\overline{E} = 0$ with Spot-E, the theory is incapable of predicting the jet axis centerline as the experimental results did not match the predicted theoretical data. This disagreement is thought to be a result of the additional elastic stresses which act in a suspended jet of Spot-E stretched in steady state. The theory, which is purely viscous, does not result in such suspended configurations because it does not account for the elastic stresses, assuming viscous Newtonian fluid.

Two corresponding cases with the imposed E.F. of 2.5 kV/mm are depicted in Fig. 20. Fig. 20a and b reveal that the electric field is capable to pull the jet back to its almost straight configuration above the 'boundary layer' swept by the belt. Because insignificant elastic stresses are expected in this case, the theory could potentially yield more plausible predictions. Indeed, the centerlines predicted with both $\overline{E} = 0.5$ and $\overline{E} = 0.1$ look plausible, while those with the higher values of $\overline{E}$ would have an exaggerated effect on the jet evolution within the E.F. It should be emphasized that in the present experiments the value of the electric charge carried by the unit length of the jet $e_0$ is unknown, and thus, the value of the dimensionless group $\overline{E}$ given by Eq. (63) cannot be calculated independently, even though the E.F. strength is known. Accordingly, several values of $\overline{E}$ were tested in Fig. 20 reveling the most plausible ones based on the background of experimental data.

## 5. Conclusion

The present experimental and theoretical results reveal that an electric field, strategically generated near a printing nozzle, can be used to enhance the DIW process, allowing orders of magnitude faster printing speed and successful printing on super rough surfaces which were conventionally impossible. The accurate and repeatable jetting enhancement was achieved utilizing the Coulomb force imposed by the electric field oriented in the direction of printing. This approach, first applied in this work to a translating belt system with a fixed nozzle, allowed a high-speed camera to visualize changes in the extruded ink jets. Next, a commercially available printer was modified in this work by the inclusion of a leading electric field acting on a photo-initiated ink Spot-E. Specifically, the addition of a single electrode to the printhead was able to increase the print speed while achieving a higher printing resolution and enabling printing on super rough substrates. With no grounded electrode or grounded substrate required in the present case, the benefits gained from the E.F. will not diminish with an increase in the build height. The present innovative approach holds great promise for (i) a significant increase in the overall build speed and throughput while maintaining or even enhancing the resolution, and (ii) a further increase in versatility of nozzle-based printing methods by expanding substrate choices previously limited or excluded due to their roughness. (iii) Multiple inks used in direct ink writing are viscous Newtonian fluids, similar to the model inks used in the present research. The approach developed here can be extended to polymeric inks which possess significant elasticity in uniaxial elongation in addition to viscosity, albeit do not differ much in their electrical conductivity from the present inks, because conductivity is fully determined by the solvent.

## Declaration of Competing Interest

The authors declare that they have no known competing financial interests or personal relationships that could have appeared to influence the work reported in this paper.

## Acknowledgment

This project was supported by National Science Foundation (NSF) Grant 1825626.

## References

[1] J. Moulson, S. Green, Effect of ambient air on liquid jet dispensing on a moving substrate, Phys. Fluids 25 (2013) 2106–2110.
[2] I. Gibson, D. Rosen, B. Stucker, Additive Manufacturing Technologies. 3D Printing, Rapid Prototyping, and Direct Digital Manufacturing, Springer, Heidelberg, 2013.
[3] E. Pei, M. Monzón, A. Bernard, Additive Manufacturing – Developments in Training and Education, Springer, Heidelberg, 2018.

[4] S. Srivatsan, T. Sudarshan, Additive Manufacturing: Innovations, Advances, and Applications, CRC Press, Boca Raton, 2015.
[5] U. Kalsoom, P. Nesterenko, B. Paull, Recent developments in 3D printable composite materials, RSC Adv. 6 (2016) 60355–60371.
[6] K.B. Hon, L. Li, I. Hutchings, Direct writing technology—advances and developments, CIRP Ann. 57 (2008) 601–620.
[7] C. Zhu, T. Han, B. Duoss, A. Golobic, J. Kuntz, C. Spadaccini, M. Worsley, Highly compressible 3D periodic graphene aerogel microlattices, Nat. Commun. 6 (2015) 6962.
[8] K. Fu, Y. Wang, C. Yan, Y. Yao, Y. Chen, J. Dai, S. Lacey, Y. Wang, J. Wan, T. Li, Graphene oxide-based electrode inks for 3D-printed lithium-ion batteries, Adv. Mater. 28 (2016) 2587–2594.
[9] A.L. Yarin, J.B. Szczech, C.M. Megaridis, J. Zhang, D.R. Gamota, Lines of dense nanoparticle colloidal suspensions evaporating on a flat surface: formation of non-uniform deposits, J. Colloid Interface Sci. 294 (2006) 343–354.
[10] D. Chrisey, A. Piqué, Introduction to Direct-Write Technologies for Rapid Prototyping, (pp.1-16). Academic Press, San Diego, 2002.
[11] P. Jiang, Z. Ji, X. Zhang, Z. Liu, X. Wang, Recent advances in direct ink writing of electronic components and functional devices, Prog. Addit. Manuf. 10 (2017) 17–35.
[12] A. Arzate, P. Tanguy, Hydrodynamics of liquid jet application in high speed coating flows, Chem. Eng. Res. Des. 83 (2005) 111–125.
[13] A.L. Yarin, Drop impact dynamics: Splashing, spreading, receding, bouncing... Annu. Rev. Fluid Mech. 159 (2006) 160–177.
[14] O. Povarov, I. Nazarov, L. Ignat, A. Nikol, Interaction of drops with boundary layer on rotating surfaces, J. Eng. Phys. 31 (1976) 1453–1456.
[15] B. Derby, Inkjet printing of functional and structural materials: fluid property requirements, feature stability, and resolution, Annu. Rev. Mater. Res. 40 (2010) 395–414.
[16] J. Boley, E. White, G. Chiu, R. Kramer, Direct writing of gallium-indium alloy for stretchable electronics, Adv. Funct. Mater. 24 (2014) 3501–3507.
[17] X. Yang, V. Chhasatia, J. Shah, Y. Sun, Coalescence, evaporation and particle deposition of consecutively printed colloidal drops, Soft Matter 8 (2012) 9205–9213.
[18] M. He, Q. Zhang, X. Zeng, D. Cui, J. Chen, H. Li, J. Wang, Y. Song, Hierarchical porous surface for efficiently controlling microdroplets' selfremoval, Adv. Mater. 25 (2013) 2291–2295.
[19] M. Kuang, L. Wang, Y. Song, Controllable printing droplets for high resolution patterns, Adv. Mater. 26 (2014) 6950–6958.
[20] M. Singh, H. Haverinen, P. Dhagat, G. Jabbour, Inkjet printing process and its applications, Adv. Mater. 22 (2010) 673–685.
[21] Y. Jiang, S. Hu, Y. Pan, A normalized trace geometry modeling method with bulge-free analysis for direct ink writing process planning, 3D Print. Addit. Manuf. 5 (2018) 301–310.
[22] J. Wang, Z. Zheng, H. Li, W. Huck, H. Sirringhaus, Dewetting of conducting polymer inkjet droplets on patterned surfaces, Nat. Mater. 3 (2010) 171–176.
[23] S. Vunnam, K. Ankireddy, J. Kellar, W. Cross, Surface modification of indium tin oxide for direct writing of silver nanoparticulate ink micropatterns, Thin Solid Films 531 (2013) 294–301.
[24] Y. Zheng, Q. Zhang, J. Liu, Pervasive liquid metal based direct-writing electronics with roller-ball pen, AIP Adv. 3 (2013), 112117.
[25] E. Feilden, E. Blanca, F. Giuliani, E. Saiz, L. Vandeperre, Robocasting of structural ceramic parts with hydrogel inks, J. Eur. Ceram. Soc. 36 (2016) 2525–2533.
[26] I. Liashenko, J. Rosell-Llompart, A. Cabot, Ultrafast 3D printing with submicrometer features using electrostatic jet deflection, Nat. Commun. 11 (2020) 753.
[27] G.I. Taylor, Disintegration of water drops in an electric field, Proc. R. Soc. Lond. A280 (1967) 383–397.
[28] A.L. Yarin, S. Koombhongse, D. Reneker, Taylor cone and jetting from liquid droplets in electrospinning of nanofibers, J. Appl. Phys. 90 (2001) 4836–4846.
[29] S. Reznik, A.L. Yarin, A. Theron, E. Zussman, Transient and steady shapes of droplets attached to a surface in a strong electric field, J. Fluid Mech. 516 (2004) 349–377.
[30] J.A. Lewis, Direct ink writing of 3D functional materials, Adv. Funct. Mater. 16 (2006) 2193–2204.
[31] T. Phung, S. Kim, K. Kwon, A high speed electrohydrodynamic (EHD) jet printing method for line printing, Micromech. Microeng. 27 (2017), 095003.
[32] A.L. Yarin, Free Liquid Jets and Films: Hydrodynamics and Rheology, Longman Scientific & Technical and John Wiley & Sons, Harlow, New York, 1993.
[33] H. Schlichting, Boundary Layer Theory, McGraw-Hill, New York, 1979.
[34] M. van Dyke, Perturbation Methods in Fluid Mechanics, Academic Press, New York, 1964.